

The Geometric Phase Appears in the Ultracold Hydrogen Exchange Reaction

B. K. Kendrick,¹ Jisha Hazra,² and N. Balakrishnan²

¹Theoretical Division (T-1, MS B221), Los Alamos National Laboratory, Los Alamos, New Mexico 87545, USA*

²Department of Chemistry, University of Nevada, Las Vegas, Nevada 89154, USA

Quantum reactive scattering calculations for the hydrogen exchange reaction $\text{H} + \text{H}_2(v = 4, j = 0) \rightarrow \text{H} + \text{H}_2(v', j')$ and its isotopic analogues are reported for ultracold collision energies. Due to the unique properties associated with ultracold collisions, it is shown that the geometric phase effectively controls the reactivity. The rotationally resolved rate coefficients computed with and without the geometric phase are shown to differ by up to four orders of magnitude. The effect is also significant in the vibrationally resolved and total rate coefficients. The dynamical origin of the effect is discussed and the large geometric phase effect reported here might be exploited to control the reactivity through the application of external fields or by the selection of a particular nuclear spin state.

In the Born-Oppenheimer description of molecules the electronic Schrödinger equation is solved to obtain an effective potential energy surface (PES) which is then used in the solution of the nuclear motion Schrödinger equation. The electronic PES often becomes degenerate with an excited electronic state resulting in a conical intersection (CI). As noted long ago by Longuet-Higgins[1] and Herzberg and Longuet-Higgins,[2] the electronic wave functions associated with a CI change sign for any nuclear motion pathway which encircles the CI (i.e., they are double-valued). The electronic sign change implies that a corresponding sign change must also occur on the nuclear motion wave function. Mead and Truhlar[3] showed that this can be accomplished by including an effective vector potential in the nuclear motion Hamiltonian. Mead[4] originally referred to this effect as the “Molecular Aharonov-Bohm” effect but it is now commonly referred to as the “geometric phase” or “Berry’s phase” effect.[5, 6]

The most studied of all chemical reactions is the hydrogen exchange reaction $\text{H} + \text{H}_2 \rightarrow \text{H} + \text{H}_2$ and its isotopic analogues $\text{H} + \text{HD} \leftrightarrow \text{D} + \text{H}_2$ and $\text{D} + \text{HD} \leftrightarrow \text{H} + \text{D}_2$. The H_3 system exhibits a CI between the ground and first excited electronic states for equilateral triangle (i.e., D_{3h}) geometries. As first predicted by Mead, the GP alters the relative sign between the reactive and non-reactive scattering amplitudes for the $\text{H} + \text{H}_2$ reaction which significantly alters the angular dependence of the differential cross sections (DCSs).[7, 8] Unfortunately, state-resolved experiments for $\text{H} + \text{H}_2$ are very difficult in practice and Mead’s predictions have not yet been verified. Though the isotopic variants are more accessible experimentally, theoretical calculations showed negligible GP effects for a wide range of collision energies.[9–17] Some relatively small rapidly varying oscillations in the DCS due to the GP have been seen in the theoretical DCSs at energies below that of the CI.[13, 18, 19] At energies above the CI, large GP effects on the DCS’s were observed which give rise to broader bi-modal features.[18–20] However,

GP effects remained elusive in the integral cross sections or reaction rates at any energy. A recent experimental attempt to measure the GP oscillations in the DCSs for the $\text{H} + \text{HD} \rightarrow \text{H} + \text{HD}$ reaction at energies below the CI was unsuccessful.[21]

Until recently,[22] all previous theoretical predictions of GP effects on chemical reactivity and experimental attempts at its detection have been done at thermal energies. Recent experimental progress in the cooling and trapping of molecules presents a novel energy regime at sub-Kelvin temperatures to explore GP effects in chemical reactions.[23, 24] In the zero-temperature limit where only s -wave contributes, the reaction rates obey the well known Bethe-Wigner threshold laws and approach finite measurable values.[25, 26] In this Letter, it is shown that due to the unique properties associated with ultracold collisions, namely: (1) isotropic scattering, and (2) quantized scattering phase shifts, the maximal possible interference between the different scattering pathways around a CI becomes possible. The maximal interference effects are shown to occur in the fundamental hydrogen exchange reaction which results in very large GP effects effectively turning on or off the reactivity. The quantized scattering phase shifts are a general property of ultracold collisions and can occur for interaction potentials which support bound states[22] as well as those which do not (as demonstrated in this Letter for the H_3 system). In the latter case, suitable vibrational excitation of the reactant diatomic molecule is required which results in an effective reaction pathway (along the vibrational adiabat) that is barrierless[27] and exhibits a potential well.[28–30]

Figure 1 plots a 2D slice of the 3D ground state H_3 electronic PES[31] and reaction pathways for the $\text{D} + \text{HD} \rightarrow \text{D} + \text{HD}$ (panel a) and $\text{D} + \text{HD} \rightarrow \text{H} + \text{D}_2$ (panel b) reactions. Hyperspherical coordinates are used which have the advantage of showing all arrangement channels simultaneously as well as the prominent CI located near the center of the plot.[32] Figure 1 corresponds to a stereographic projection of the upper half of the hypersphere with a fixed hyperradius of $\rho = 3.75 a_0$. The zero of energy is the bottom of the asymptotic $\text{H} + \text{D}_2$ potential well. The contour lines are separated by 2,900 K ex-

* Correspondence should be addressed to BKK (bkendric@lanl.gov).

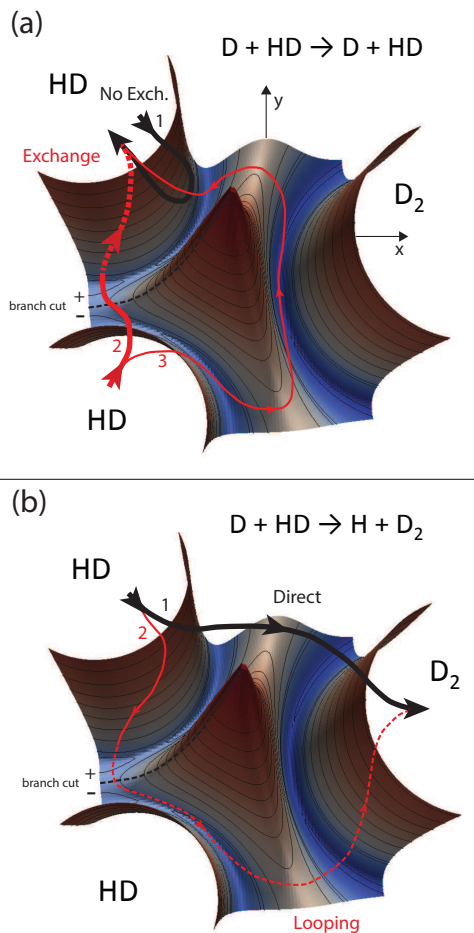


FIG. 1. (color online) A 2D slice of the 3D Born-Oppenheimer PES for the HD_2 system is plotted at a fixed hyperradius $\rho = 3.75 a_0$. The different scattering pathways around the CI are indicated, panel (a) for $\text{D} + \text{HD} \rightarrow \text{D} + \text{HD}$, and panel (b) for $\text{D} + \text{HD} \rightarrow \text{H} + \text{D}_2$. For clarity, pathways for only one of the symmetric HD channels is depicted (see text for discussion).

cept for the two closely spaced contours at 4,640 K and 5,220 K. For clarity, a cut-plane is used at 33,640 K so that the extremely repulsive regions for each channel are not plotted. The energy of the CI in Fig. 1 is 37,700 K and the PES for the excited electronic state is not plotted.

The two panels in Figure 1 depict the interference pathways which can lead to significant GP effects for each reaction. In general the total scattering amplitude can be decomposed into contributions from each pathway labeled by the 1, 2, and 3 in panels (a) and (b).[7, 14–16] For the inelastic scattering in 1 (a), pathway #1 (black) corresponds to a non-reactive process and pathways #2 and #3 (red) corresponds to an exchange process where the two identical D nuclei in each HD channel are exchanged. For the reactive scattering in 1 (b), pathway #1 (black) corresponds to a direct reaction process and pathway #2 (red) corresponds to a looping reaction pro-

cess. For the D-atom exchange in 1 (a), it has been shown that, due to the direct collinear nature of the reaction, contributions from pathway #3 (thin red curve) are negligible even for high collision energies approaching that of the CI.[9–14] Thus, the total scattering amplitude which does not include the GP can be written as $\tilde{f}^{\text{NGP}} = (1/\sqrt{2})(\tilde{f}_1 + \tilde{f}_2)$ where NGP denotes “No Geometric Phase” and \tilde{f}_1 and \tilde{f}_2 are the scattering amplitudes for pathways #1 and #2 in Fig. 1 (a).[7, 14–16] The GP alters the sign on the scattering amplitude for pathway #2 across the branch cut (black dashed curve in Fig. 1). Thus, the total scattering amplitude which includes the GP is given by $\tilde{f}^{\text{GP}} = (1/\sqrt{2})(\tilde{f}_1 - \tilde{f}_2)$ where GP denotes “with Geometric Phase”.[7, 14–16] The same expressions hold for the NGP and GP scattering amplitudes in Fig. 1 (b).[14–16] The encirclement of the CI by the combined pathways #1 and #2 is obvious in Fig. 1 (b) but not so obvious in Fig. 1 (a). Pathway #2 in Fig. 1 (a) encircles the CI through “symmetric encirclement” (i.e., via the symmetrization of the wave function with respect to permutation of the identical D nuclei).[3, 7, 14–16]

The cross sections and rate coefficients are computed from the square modulus of the total scattering amplitude $\|\tilde{f}\|^2 = (1/2)(f_1^2 + f_2^2 \pm 2f_1f_2\cos\Delta)$ where the + and – denote NGP and GP, respectively. The complex scattering amplitudes are expressed as $\tilde{f}_1 = f_1 \exp(i\delta_1)$, $\tilde{f}_2 = f_2 \exp(i\delta_2)$ and the phase difference $\Delta = \delta_2 - \delta_1$. If the square modulus of the scattering amplitude for one of the pathways is much larger than the other: $f_1^2 \gg f_2^2$ or $f_2^2 \gg f_1^2$, then the square modulus of the total scattering amplitude is given by $\|\tilde{f}\|^2 \approx f_1^2/2$ or $\|\tilde{f}\|^2 \approx f_2^2/2$, respectively, and the GP effect is negligible. However, when the squared moduli are similar $f_1^2 \approx f_2^2$, then $\|\tilde{f}\|^2 \approx f^2(1 \pm \cos\Delta)$ where $f = f_1 \approx f_2$. Thus, depending upon the sign and magnitude of $\cos\Delta$, the reactivity can be dramatically enhanced or suppressed. The maximum interference occurs when $|\cos\Delta| = 1$. If $\pm \cos\Delta = +1$ then maximum constructive interference occurs and $\|\tilde{f}\|^2 \approx 2f^2$, whereas for $\pm \cos\Delta = -1$, maximum destructive interference occurs and $\|\tilde{f}\|^2 \approx 0$. That is, if $|\cos\Delta| \approx 1$ then the reactivity can be turned on or off by the sign of the interference term. Since the GP alters the sign of the interference term, the GP effectively controls the reactivity.

The quantum reactive scattering calculations for the H_3 system were done using a numerically exact time-independent coupled-channel method based on hyperspherical coordinates and the GP effect is included using the vector potential approach.[12, 32–36] The computed scattering (S) matrices include all open reactant and product diatomic vibrational and rotational states on a grid consisting of 112 collision energies spanning the range from $1 \mu\text{K}$ to 4,640 K relative to asymptotic energy of $\text{HD}(v = 4, j = 0)$ for the $\text{H} + \text{HD}$ and $\text{D} + \text{HD}$ reactions, and $\text{H}_2(v = 4, j = 0)$ for $\text{H} + \text{H}_2$. For the highly excited reactant vibrational states, the

reaction becomes effectively barrierless and exhibits significant reactivity at ultracold collision energies.[27] The asymptotic energies for $\text{HD}(v=4, j=0)$ and $\text{H}_2(v=4, j=0)$ are 22, 109 K and 25, 078 K relative to the bottom of the asymptotic diatomic potential wells, respectively. The scattering calculations were carried out using two accurate *ab initio* electronic PESs for the H_3 system: the BKMP2[31] and the newer one by Mielke, et al.[37]

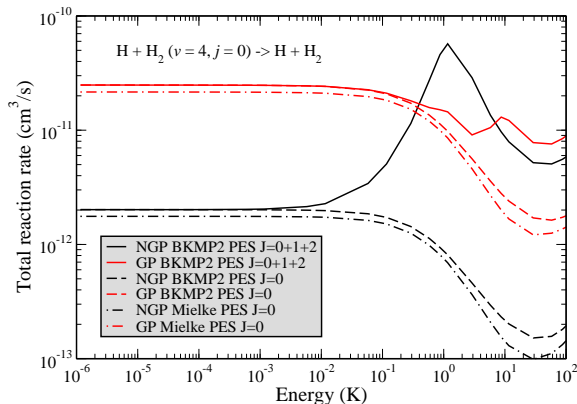


FIG. 2. (color online) The total reaction rate for the $\text{H} + \text{H}_2(v=4, j=0) \rightarrow \text{H} + \text{H}_2$ (para-para) reaction is plotted as a function of collision energy (see text for discussion).

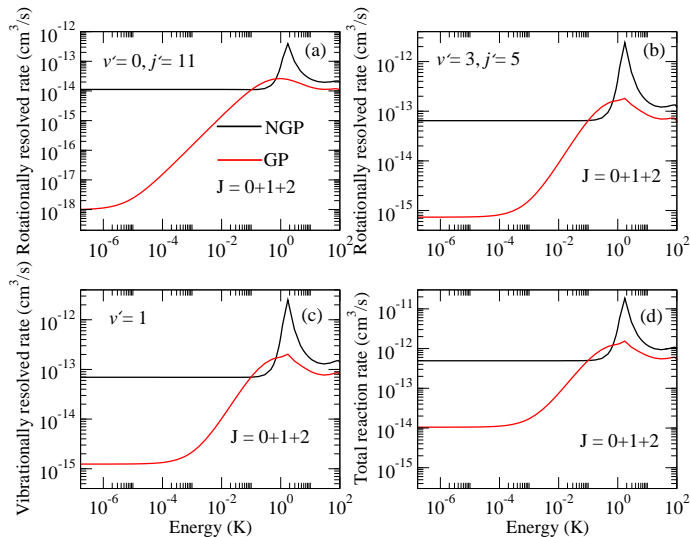


FIG. 3. (color online) Reaction rates for the $\text{D} + \text{HD}(v=4, j=0) \rightarrow \text{D} + \text{HD}(v', j')$ reaction are plotted as a function of collision energy: (a) $v'=0, j'=11$, (b) $v'=3, j'=5$, (c) $v'=1$, and (d) total. The results are for even exchange symmetry and include all values of total angular momentum $J=0-2$ (see text for discussion).

Figure 2 plots the total reaction rate for $\text{H} + \text{H}_2(v=4, j=0) \rightarrow \text{H} + \text{H}_2$ summed over all product vibrational and even rotational states (i.e., the para-para transi-

tions). The results which include (do not include) the GP are plotted in red (black). The thick curves include all values of total angular momentum $J=0-2$ and the thinner curves are for $J=0$ only. The rates for each value of J are well converged over the entire energy range. The total rate is well converged with respect to the sum over $J=0-2$ up to about 2 K.[36] The dashed and long-short dashed curves compare the results based on the BKMP2 and Mielke PES, respectively. Both PESs give similar results and predict that the GP enhances the ultracold reactivity by a full order of magnitude. Figure 3 plots several representative rate coefficients for the $\text{D} + \text{HD}(v=4, j=0) \rightarrow \text{D} + \text{HD}(v', j')$ reaction using the BKMP2 PES. The rates are computed for even exchange symmetry (i.e., the nuclear motion wave function is symmetric with respect to permutation of the identical D nuclei) and include all values of total angular momentum $J=0-2$. The rotationally resolved rate for $v'=0, j'=11$ shows that the geometric phase reduces the reactivity by over four orders of magnitude. The rate for $v'=3, j'=5$ and the vibrationally resolved rate for $v'=1$ are reduced by nearly two orders of magnitude when the GP is included. The total rate which includes the GP is reduced by a factor of 50. The rates for odd exchange symmetry are similar in magnitude except that the GP increases the reactivity in this case.[36] When both the symmetric and antisymmetric nuclear spin states of D_2 are present, the scattering results must be summed over both even and odd exchange symmetries including the appropriate nuclear spin statistical weights $2/3$ and $1/3$, respectively. The GP effect is reduced but remains significant (see Table I and Ref. 36).

Table I lists a representative sample of the ultracold ($1\mu\text{K}$) reaction rates computed for the H_3 system both with and without the geometric phase and different exchange symmetries. Most notable are the very large GP effects seen in the rotationally resolved rates for the $\text{D} + \text{HD} \rightarrow \text{D} + \text{HD}$ reaction for each exchange symmetry. These differences persist, albeit smaller when summed over both exchange symmetries. The GP effects for the $\text{H} + \text{HD} \rightarrow \text{H} + \text{HD}$ reaction are overall smaller than those for the $\text{D} + \text{HD}$ reaction. For the $\text{H} + \text{H}_2 \rightarrow \text{H} + \text{H}_2$ para-para reaction, the results have already been summed over the appropriate nuclear spin states. Large differences ($\approx 10x$) between the GP and NGP rates are observed even when summed over all v' and j' . The total rates summed over all v' and j' using the PES of Mielke et al. are tabulated in the last column. They are very similar at the state resolved level as well but the overall reactivity is slightly reduced (see Fig. 2). For the $\text{D} + \text{HD} \rightarrow \text{H} + \text{D}_2$ and $\text{H} + \text{HD} \rightarrow \text{D} + \text{H}_2$ reactions (not tabulated), the GP and NGP rates are nearly identical even at the rotationally resolved and single exchange symmetry level. The same applies to the $\text{H} + \text{H}_2$ para-ortho reaction (not tabulated). The lack of GP effects for these ultracold reactions is due to the direct collinear nature of the reaction which results in a tiny contribution

TABLE I. Ultracold ($1\mu\text{K}$) reaction rates for the $X + \text{HD}(v = 4, j = 0) \rightarrow X + \text{HD}(v', j')$ with $X=\text{D}$ and H , and the $\text{H} + \text{H}_2(v = 4, j = 0) \rightarrow \text{H} + \text{H}_2(v', j' \text{ even})$ reactions. The “evn” and “odd” denote exchange symmetry and the “GP” and “NGP” denote the results computed with and without the geometric phase, respectively. The “(evn) + (odd)” denote the summed results over even and odd exchange symmetry. All rates include the appropriate nuclear spin statistical weights and are in cm^3/s .

Reaction	$v'=0, j'=11$	$v'=2, \sum_{j'}$	Total	Mielke PES
D + HD(evn) GP	1.01(-18)	1.51(-15)	1.05(-14)	6.64(-15)
	1.13(-14)	1.52(-13)	4.94(-13)	2.51(-13)
D + HD(odd) GP	5.48(-15)	7.52(-14)	2.44(-13)	1.25(-13)
	1.90(-19)	7.42(-16)	4.99(-15)	2.97(-15)
(evn) + (odd) GP	5.48(-15)	7.67(-14)	2.54(-13)	1.32(-13)
	1.13(-14)	1.53(-13)	4.98(-13)	2.54(-13)
	$v'=0, j'=2$	$v'=0, \sum_{j'}$		
H + HD(evn) GP	1.60(-17)	1.58(-14)	9.87(-14)	
	1.22(-14)	8.80(-14)	3.15(-13)	
H + HD(odd) GP	3.79(-14)	2.71(-13)	9.35(-13)	
	1.95(-17)	4.34(-14)	2.85(-13)	
(evn) + (odd) GP	3.79(-14)	2.87(-13)	1.03(-12)	
	1.22(-14)	1.31(-13)	6.00(-13)	
	$v'=3, j'=4$	$v'=3, \sum_{j'}$		
H + H ₂ GP	4.32(-11)	8.39(-12)	2.48(-11)	2.16(-11)
	2.16(-13)	5.41(-13)	2.02(-12)	1.76(-12)

from the scattering amplitude corresponding to looping pathway in Fig. 1 (b).

For ultracold collisions of H or D with a high vibrationally excited HD or H₂ diatomic molecule, leading to vibrational quenching, the reaction pathway is effectively barrierless with an attractive potential well.[27–30] Thus, each scattering pathway in Fig. 1 can be represented by a simple 1D spherical well model. For this 1D model, the scattering phase shifts are known analytically and in the zero energy limit they become effectively quantized (i.e., they approach $n\pi$ where n denotes the number of bound states in 1D spherical well).[22, 36] If the number of bound states in the two different 1D spherical well po-

tentials corresponding to the two reaction pathways in Fig. 1(a) differ by an even (odd) number, then $\cos \Delta = 1$ ($\cos \Delta = -1$). Maximum constructive (destructive) interference will occur between the two scattering amplitudes contributing to \hat{f}^{NGP} , and the opposite interference behavior will occur for \hat{f}^{GP} . Thus, the unusually large GP effects reported here originate from the isotropic (s -wave) scattering and the effective quantization of the scattering phase shift which results in $|\cos \Delta| \approx 1$. [22, 36] The mechanism is general and is expected to hold for many molecules which exhibit CIs and for which the PES and/or the choice of reactant and product states allows for a favorable encirclement.[22]

We emphasize that the interference mechanism reported here is a general property of ultracold collisions and will also occur in molecules without CIs or GP effects. In general, large interference effects can be expected for barrierless reaction paths which proceed over a potential well (due to the PES or vibrational excitation) and include contributions from two interfering pathways (such as reactive and non-reactive). Experimentally the interference (and hence reactivity) might be controlled by the selection of a specific nuclear spin state or by the application of external electric or magnetic fields to (1) alter the relative number of bound states in the effective potential wells along each interfering pathway, or (2) alter the relative magnitude of the two interfering scattering amplitudes.

Acknowledgments

BKK acknowledges that part of this work was done under the auspices of the US Department of Energy under Project No. 20140309ER of the Laboratory Directed Research and Development Program at Los Alamos National Laboratory. Los Alamos National Laboratory is operated by Los Alamos National Security, LLC, for the National Security Administration of the US Department of Energy under contract DE-AC52-06NA25396. The UNLV team acknowledges support from the Army Research Office, MURI grant No. W911NF-12-1-0476 and the National Science Foundation, grant No. PHY-1205838.

- H. C. Longuet-Higgins, U. Öpik, M. H. L. Pryce, and R. A. Sack, *Proc. R. Soc. London, Ser. A* **244**, 1 (1958).
- G. Herzberg and H. C. Longuet-Higgins, *Discuss. Faraday Soc.* **35**, 77 (1963).
- C. A. Mead and D. G. Truhlar, *J. Chem. Phys.* **70**, 2284 (1979); **78**, 6344E (1983).
- C. A. Mead, *Chem. Phys.* **49**, 23 (1980).
- M. V. Berry, *Proc. R. Soc. London Ser. A* **392**, 45 (1984).
- A. Bohm, *Quantum Mechanics: Foundations and Applications*, 3rd Edition, (Springer-Verlag, New York), Chapters XII and XIII, (1993), (2001).
- C. A. Mead, *J. Chem. Phys.* **72**, 3839 (1980).
- B. Lepetit, A. Kuppermann, *Chem. Phys. Lett.* **166**, 581 (1990).
- B. K. Kendrick, *J. Chem. Phys.* **112**, 5679 (2000); **114**, 4335E (2001).
- B. K. Kendrick, *J. Chem. Phys.* **114**, 8796 (2001).
- B. K. Kendrick, *J. Chem. Phys.* **118**, 10502 (2003).
- B. K. Kendrick, *J. Phys. Chem.* **107**, 6739, (2003).
- C. Juanes-Marcos, S. C. Althorpe, *J. Chem. Phys.* **122**, 204324 (2005).
- J. C. Juanes-Marcos, S. C. Althorpe and E. Wrede, *Science* **309**, 1227 (2005).
- S. C. Althorpe, *J. Chem. Phys.* **124**, 084105 (2006).
- S. C. Althorpe, T. Stecher, and F. Bouakline, *J. Chem. Phys.* **129**, 214117 (2008).
- F. Bouakline, *Chem. Phys.* **442**, 31-40 (2014).
- F. Bouakline, B. Lepetit, S. C. Althorpe, and A. Kuppermann, in “The Jahn-Teller effect fundamentals and implications for physics and chemistry”, Castleman, Jr.,

- A. P., Toennies, J. P., Yamanouchi, K., & Zinth, W. Eds. *Springer Series in Chemical Physics*, **97**, 201-237 (2009).
19. F. Bouakline, S. C. Althorpe, and D. P. Ruiz, *J. Chem. Phys.* **128**, 124322 (2008).
 20. F. Bouakline, S. C. Althorpe, P. Larregaray, and L. Bonnet, *Molec. Phys.* **108**, 969-980 (2010).
 21. J. Jankunas, M. Sneha, R. N. Zare, F. Bouakline, and S. C. Althorpe, *J. Chem. Phys.* **139**, 144316 (2013).
 22. B. K. Kendrick, J. Hazra and N. Balakrishnan, *Nat. Commun.* in press.
 23. L. D. Carr, D. DeMille, R. V. Krems, J. Ye, *New J. Phys.* **11**, 055049 (2009).
 24. S. Ospelkaus *et al.*, *Science* **327**, 853 (2010).
 25. H. A. Bethe, *Phys. Rev.* **47**, 747 (1935).
 26. E. P. Wigner, *Phys. Rev.* **73**, 1002 (1948).
 27. I. Simbotin, S. Ghosal, and R. Côté, *Phys. Chem. Chem. Phys.* **13**, 19148 (2011).
 28. W. H. Miller, N. C. Handy, and J. E. Adams, *J. Chem. Phys.* **72**, 99 (1980).
 29. D. G. Truhlar, B. C. Garrett, and J. S. Klippenstein, *J. Phys. Chem.* **100**, 12771 (1996).
 30. J. Jankunas, M. Sneha, R. N. Zare, F. Bouakline, S. C. Althorpe, D. Herráez-Aguilar, and F. J. Aoiz, *PNAS* **111**, 15 (2014).
 31. A. I. Boothroyd, W. J. Keogh, P. G. Martin, and M. R. Peterson, *J. Chem. Phys.* **104**, 7139 (1996).
 32. R. T Pack, G. A. Parker, *J. Chem. Phys.* **87**, 3888 (1987).
 33. B. Kendrick and R. T Pack, *J. Chem. Phys.* **104**, 7475 (1996).
 34. B. K. Kendrick, R. T Pack, R. B. Walker and E. F. Hayes, *J. Chem. Phys.* **110**, 6673 (1999).
 35. C. Makrides *et al.*, *Phys. Rev. A* **91**, 012708 (2015).
 36. See the online supplementary material for more details.
 37. S. L. Mielke, B. C. Garrett, and K. A. Peterson, *J. Chem. Phys.* **116**, 4142 (2002).

SUPPLEMENTARY MATERIAL

The three-body quantum reactive scattering methodology is based on a time-independent coupled-channel approach using hyperspherical coordinates[32] and is well suited for treating ultracold collisions.[35] The method is numerically exact and accurately treats the body-frame Eckart singularities[34] associated with non-zero total angular momentum J and includes the geometric phase using the general vector potential approach.[12, 33] A brief summary of the methodology is given here. In the interaction region where the three atoms are in close proximity (i.e., for small hyperradius ρ), Smith-Johnson symmetrized hyperspherical coordinates are used. For larger hyperradius where the reactant and product channels become well defined, a properly symmetrized set of Fock-Delves hyperspherical coordinates are used (one for each channel). The hyperradius ρ is discretized into a set of sectors spanning the range from small to large ρ . The three-body Hamiltonian is diagonalized at each fixed value of ρ to obtain a set of 2D angular wave functions. The 2D angular solutions are independent of the collision energy so only have to be computed once for each value of total angular momentum J and inversion parity. The 2D angular solutions form the basis set for the coupled-channel equations in ρ and are used to compute a set of potential coupling matrices within each sector and the overlap matrices between the different 2D solutions at the boundaries of each sector. The coupled-channel equations are solved for a given collision energy using Johnson's log-derivative propagator method from small to large ρ . Finally, the asymptotic boundary conditions are applied at large ρ to compute the scattering S matrix from which the cross sections and reaction rates can be computed.

The individual contributions from each value of total angular momentum $J = 0 - 2$ to the total reaction rate for the $D + HD(v = 4, j = 0) \rightarrow D + HD$ reaction are plotted in Fig. S1 as a function of collision energy. The results with (without) the GP are plotted in red (black). The thick red and black curves correspond to the total rate summed over all values of $J = 0 - 2$. The contributions to the rate from $J > 0$ rapidly decrease with decreasing collision energy due to the angular momentum barrier in the entrance channel which increases with J . The rates for each value of J are well converged over the entire energy range. Fig. S1 shows that the total rate summed over $J = 0 - 2$ is converged for collision energies up to about 2 K.

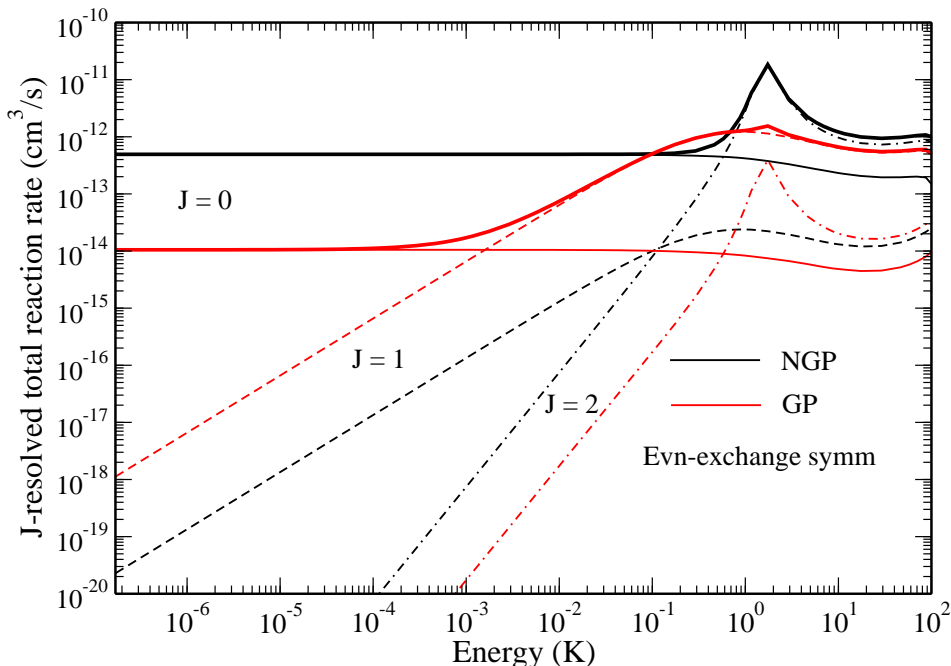


FIG. S1. The individual contributions to the total reaction rate for $D + HD(v = 4, j = 0) \rightarrow D + HD$ from each value of total angular momentum $J = 0 - 2$ are plotted (see legend). The results are for even exchange symmetry. The GP and NGP reaction rates summed over all values of $J = 0 - 2$ are shown as thick red and black curves, respectively (see text for discussion).

The reaction rates for the $D + HD(v = 4, j = 0) \rightarrow D + HD(v', j')$ reaction are plotted in Fig. S2 as a function of

collision energy for several values of v' and j' (the same as those in Fig. 3 of the main article). The rates correspond to odd exchange symmetry and include all values of total angular momentum $J = 0 - 2$. In contrast to the even exchange symmetry results plotted in Fig. 3 of the main article, it is the GP ultracold reaction rates which are largest for odd exchange symmetry. Figure S3 plots the reaction rates summed over both even (Fig. 3) and odd (Fig. S2) exchange symmetries multiplied by the appropriate nuclear spin statistical weights. The differences between the GP and NGP ultracold reaction rates are smaller but still significant.

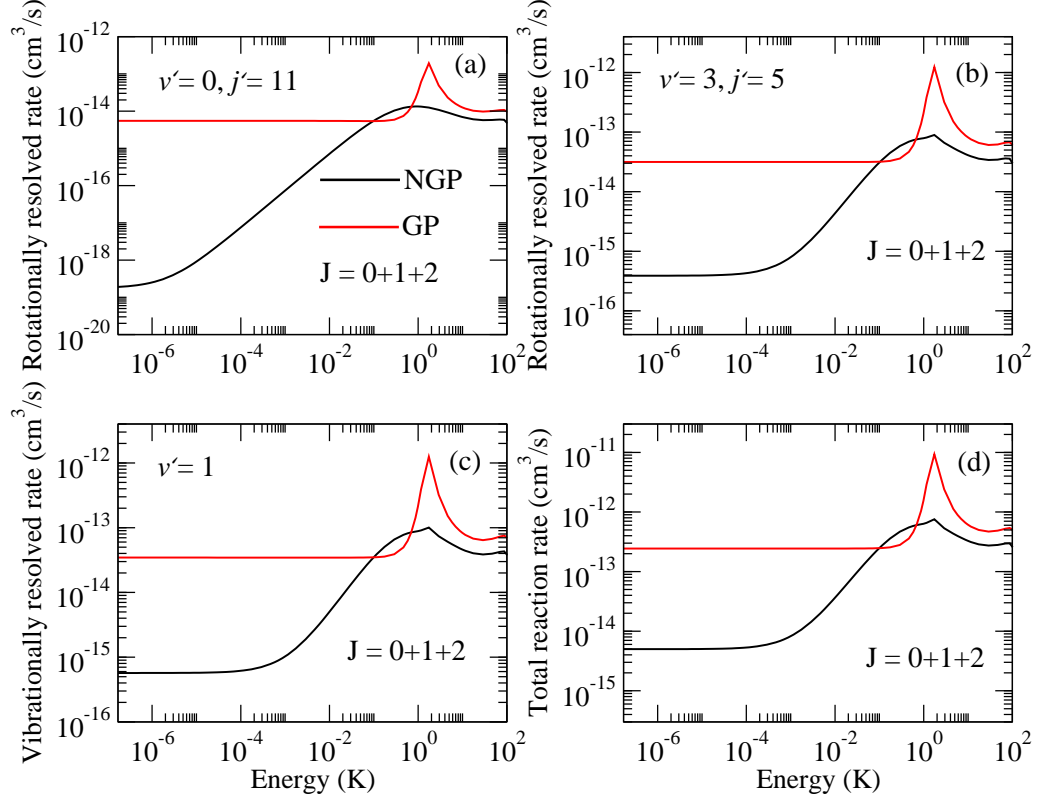


FIG. S2. Reaction rates for the $D + HD(v = 4, j = 0) \rightarrow D + HD(v', j')$ reaction are plotted as a function of collision energy: (a) $v' = 0, j' = 11$, (b) $v' = 3, j' = 5$, (c) $v' = 1$, and (d) total. The results are for odd exchange symmetry and include all values of total angular momentum $J = 0 - 2$.

Figure S4 panel (a) plots the ratio of the average square moduli of the exchange and non-reactive pathways depicted in Fig. 1 of the main article as a function of collision energy for the $D + HD(v = 4, j = 0) \rightarrow D + HD(v' = 3, j' = 5)$ reaction. The results for $J = 0, 1$, and summed over $J = 0 - 2$ are plotted in black, red, and blue, respectively. In each case, the ratio is near unity for a wide range of energies from $1 \mu\text{K}$ to 100K . This implies that maximal interference between the exchange and non-reactive pathways depicted in Fig. 1 (a) is possible, and that the interference will be governed by the sign and magnitude of $\cos \Delta$. Figure S4 panel (b) plots the average value of $\cos \Delta$ as a function of collision energy for $m_{j'} = 5$ (the results for other values of $m_{j'}$ are similar). The results for $J = 0$ and 1 show that the scattering phase difference Δ lies near an even and odd value of π , respectively. This leads to maximal interference between the non-reactive and exchange pathways in Fig. 1 (a). Since $\cos \Delta = +1$ for $J = 0$, the square moduli of the total NGP and GP scattering amplitudes are given by $\|\tilde{f}^{\text{NGP}}\|^2 = f^2 (1 + \cos \Delta) \approx 2f^2$ and $\|\tilde{f}^{\text{GP}}\|^2 = f^2 (1 - \cos \Delta) \approx 0$ which explains why the NGP ultracold reaction rates are much larger than the GP ones in Fig. 3 of the main article. For $J = 1$ the situation is reversed since $\cos \Delta = -1$. This dramatically reduces the differences between the NGP and GP reaction rates at higher collision energies when the contributions from $J = 1$ and higher J become important. As shown in Fig. S4 panel (b), at the higher collision energies (i.e., $> 1 \text{mK}$) where more values of J contribute (blue curve), the $\cos \Delta$ is no longer quantized and tends to oscillate about zero. For odd exchange symmetry, the situation is reversed and $\cos \Delta = -1$ and $+1$ for $J = 0$ and 1 , respectively. This explains why the GP ultracold reaction rates are much larger than the NGP ones in Fig. S2.

The tendency for $\cos \Delta$ to be near a multiple of π (as discussed above in the context of Fig. S4) at ultracold collision energies occurs for the majority of product states in all three exchange reactions. Figure S5 plots $\cos \Delta$ vs

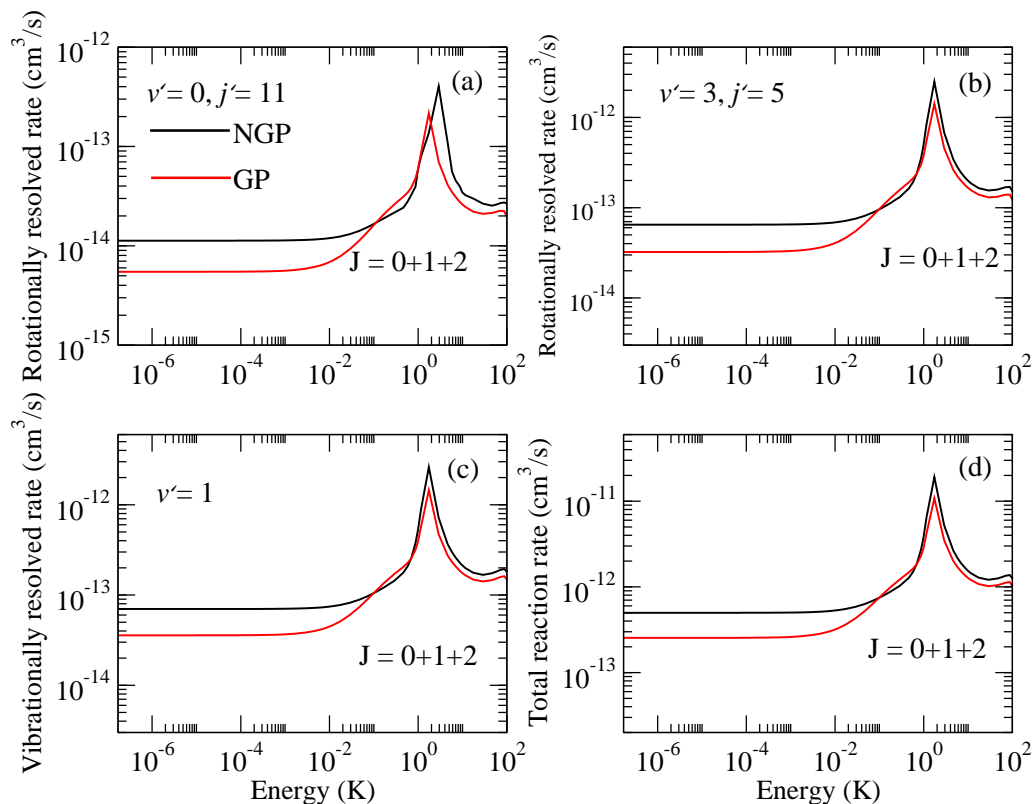


FIG. S3. Reaction rates for the $D + HD(v = 4, j = 0) \rightarrow D + HD(v', j')$ reaction are plotted as a function of collision energy: (a) $v' = 0, j' = 11$, (b) $v' = 3, j' = 5$, (c) $v' = 1$, and (d) total. The results are summed over both even and odd exchange symmetry and include all values of total angular momentum $J = 0 - 2$.

$\cos \Delta$ at the ultracold collision energy of $1 \mu\text{K}$ for the three exchange reactions: (a) $D + HD(v = 4, j = 0) \rightarrow D + HD(v', j')$, (b) $H + HD(v = 4, j = 0) \rightarrow H + HD(v', j')$, and (c) $H + H_2(v = 4, j = 0) \rightarrow H + H_2(v', j' \text{ even})$. The preference for $\cos \Delta \approx \pm 1$ is striking. The value of $\cos \Delta$ for the large majority of product states are clearly clustered at the top-right and bottom-left corners. In panels (a) and (b), the values $\cos \Delta = +1$ and -1 are preferred by the even (red) and odd (black) exchange symmetries, respectively. The quantization effect is most dramatic for the $D + HD$ reaction (panel a) and the $H + H_2$ reaction (panel c) which explains why these two reactions exhibit the largest overall GP effects relative to the $H + HD$ reaction (panel b) (see also Table I in the main article). In panel (c), the $\cos \Delta$ are plotted at three different collision energies: $1 \mu\text{K}$ (black), 1K (blue), and $100 \mu\text{K}$ (red). At higher collision energies the $\cos \Delta$ are not quantized and take on a wide range of values with $|\cos \Delta| < 0.8$. However, at the ultracold energy of $1 \mu\text{K}$ (black), the $\cos \Delta$ become essentially quantized and approach values very close to $+1$.

The dynamical origin of the phase quantization observed in Figs. S4 and S5 can be understood by considering a simple 1D spherical well potential. Figure S6 shows a 1D spherical well potential with depth V_o and radius r_o . The scattering phase shift δ can be derived analytically for this model and is given by the expression shown in Fig. S6 for s -wave scattering (i.e., $l = 0$). The analytic phase shift is plotted as a function of the wave number k and each blue curve corresponds to a different well depth V_o . In the ultracold limit $k \rightarrow 0$, the majority of the phase shifts (blue curves) converge towards a multiple of π . For very small values of k , the phase shift quickly jumps from one value of π to another as the well depth V_o is varied. The jumps occur at intervals of $\pi/2$ which correspond to resonances associated with a continuum state dropping into the well to become a bound state. In general, the phase shift for $k \rightarrow 0$ is equal to $n\pi$ where n denotes the number of bound states supported by the potential well. For high-lying vibrationally excited reactant states, the ultracold hydrogen exchange reaction is effectively barrierless[27] and proceeds along an effective attractive potential well (i.e., vibrational adiabatic).[28–30] Thus, the scattering phase shifts along each pathway depicted in Fig. 1 of the main article can be modeled using an effective 1D spherical well potential. Since each pathway has a different effective well depth V_o and radius r_o , it will support a different number of bound states and hence the ultracold scattering phase shift along each pathway will approach a different multiple of π . This implies that the phase difference Δ will also approach a multiple of π . If the multiple of π is an even or odd number, then $\cos \Delta = +1$ or $\cos \Delta = -1$, respectively. This ultimately determines whether the interference will be

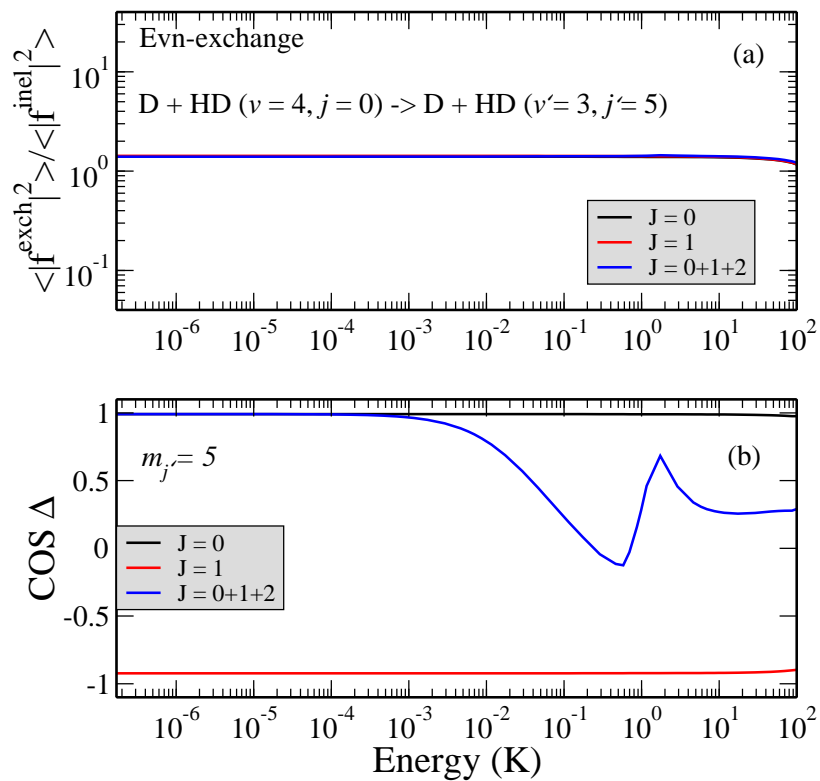


FIG. S4. In panel (a), the ratio of the average square modulus of the exchange (pathway #2 in Fig. 1 a) and non-reactive (pathway #1 in Fig. 1 a) contributions to the total scattering amplitude is plotted as a function of collision energy for the $\text{D} + \text{HD}(v=4, j=0) \rightarrow \text{D} + \text{HD}(v'=3, j'=5)$ reaction for even exchange symmetry. The black and red curves correspond to single values of $J=0$ and 1, respectively. The blue curve corresponds to the sum over all values of J between 0 and 2. Panel (b) plots the average of $\cos \Delta$ as a function of collision energy for $m_{j'}=5$ using the same color designations as in panel (a).

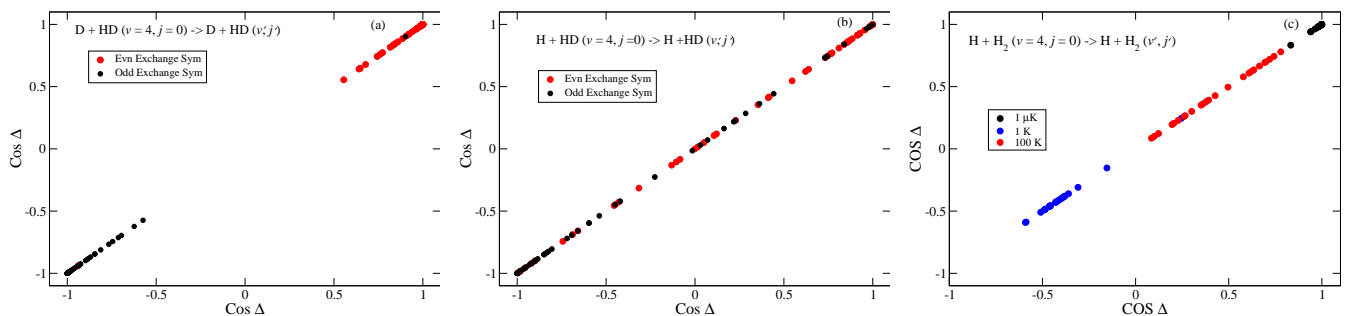


FIG. S5. The $\cos \Delta$ vs $\cos \Delta$ are plotted for three hydrogen exchange reactions. In panel (a), the results for $\text{D} + \text{HD}(v=4, j=0) \rightarrow \text{D} + \text{HD}(v', j')$ are plotted at $1 \mu\text{K}$. Each point corresponds to a v', j' product state and red (black) points correspond to even (odd) exchange symmetry. Panel (b) is similar to panel (a) except that the results are for $\text{H} + \text{HD}(v=4, j=0) \rightarrow \text{H} + \text{HD}(v', j')$. Panel (c) plots the results for $\text{H} + \text{H}_2(v=4, j=0) \rightarrow \text{H} + \text{H}_2(v', j')$ even at three different collision energies: black ($1 \mu\text{K}$), blue (1K), and red (100K).

constructive or destructive and whether the GP or NGP reaction rates will be the largest. Furthermore, the effective 1D spherical well potential associated with each of the reaction pathways also depends upon the particular reactant and product states involved (hence the distribution of points observed in Fig. S5).

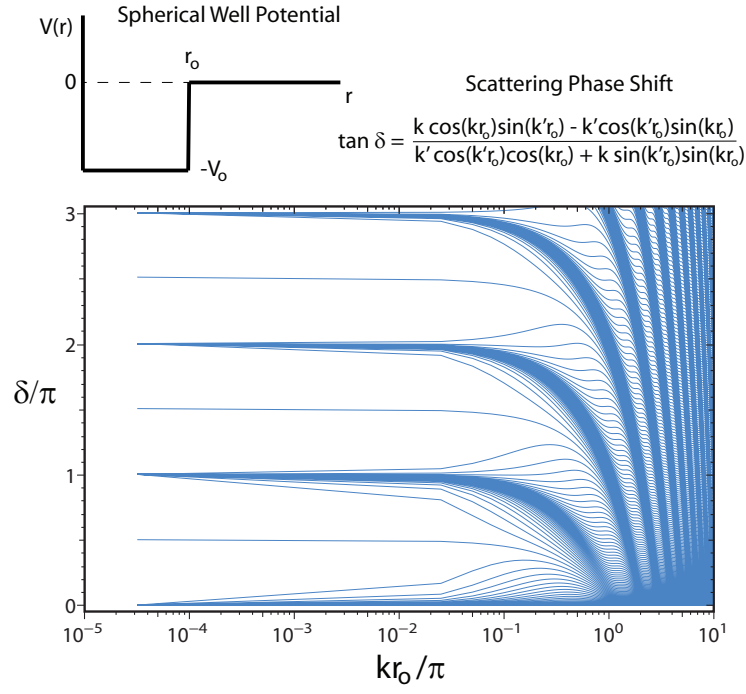


FIG. S6. The 1D spherical well potential model with depth V_o and radius r_o , and its associated scattering phase shift (for $l = 0$) are plotted. The scattering phase shifts δ in units of π are plotted as a function of the wave number in units π/r_o for different potential well depths $V_o = q^2/(2\mu)$ separated by $q = 0.025 \pi/r_o$ (blue curves) where $k'^2 - q^2 = k^2$. In the zero temperature limit $k \rightarrow 0$, the majority of scattering phase shifts approach a multiple of π (i.e., they become effectively quantized).